Available online at www.sciencedirect.com

jmr&t
Journal of Materials Research and Technology

journal homepage: www.elsevier.com/locate/jmrt

# Microstructural characterization and mechanical properties of additively manufactured 21-6-9 stainless steel for aerospace applications

*Pragya Mishra* [a,*], *Pia Åkerfeldt* [a], *Fredrik Svahn* [b], *Erik Nilsson* [a], *Farnoosh Forouzan* [a,c], *Marta-Lena Antti* [a]

[a] *Materials Science, Department of Engineering Sciences and Mathematics, Luleå University of Technology, 97187 Luleå, Sweden*
[b] *GKN Aerospace Sweden AB, 46130 Trollhättan, Sweden*
[c] *Höganäs AB, 263 39 Höganäs, Sweden*

ARTICLE INFO

*Article history:*
Received 20 April 2023
Accepted 5 June 2023
Available online 8 June 2023

*Keywords:*
L-PBF
21-6-9 stainless steel
Elevated temperature
Cryogenic temperature
Microstructural characterization
Mechanical properties

ABSTRACT

The alloy 21-6-9 is a nitrogen-strengthened austenitic stainless steel often used in aerospace applications due to its high strength, good fabrication properties, and toughness at cryogenic temperatures. However, minimal research has been conducted on alloy 21-6-9 using the additive manufacturing process laser powder-bed fusion (L-PBF). The L-PBF technique has been seen as a key to reducing production time and avoiding costly machining. Therefore, there is an interest in investigating L-PBF-processed 21-6-9 to determine the effects of L-PBF on properties at elevated and cryogenic temperatures. In this study, prior to tensile testing the alloy 21-6-9 underwent heat treatments that simulated aerospace applications and the alloy was analyzed and characterized to evaluate phase stability. The effects of elevated and cryogenic temperatures (77 K) on the tensile behavior and microstructure were investigated using X-ray diffraction (XRD) and electron backscatter diffraction (EBSD). The tensile tests showed that the yield strength and ultimate tensile strength improved, while ductility varied depending on the conditions and test environment. The ultimate tensile strength was approximately 80% higher at 77 K than at room temperature, although the elongation decreased by around 90%, possibly due to the formation of strain-induced martensite.



## 1. Introduction

Over the past decade, additive manufacturing (AM) has emerged as a revolutionary manufacturing process, particularly in the aerospace industry, offering a direct path from design to finished products without the lengthy traditional manufacturing procedures [1–3]. One of the most widely adopted AM techniques is laser powder-bed fusion (L-PBF), a subset of powder bed fusion methods. Moeinfar et al. [1] analyzed various AM techniques, highlighting Laser Additive Manufacturing (LAM) as a highly promising approach known

* Corresponding author.
E-mail addresses: pragya.mishra@ltu.se (P. Mishra), pia.akerfeldt@ltu.se (P. Åkerfeldt), fredrik.svahn@gknaerospace.com (F. Svahn), erik.1.nilsson@ltu.se (E. Nilsson), Farnoosh.Forouzan@hoganas.com (F. Forouzan), Marta-Lena.Antti@ltu.se (M.-L. Antti).
https://doi.org/10.1016/j.jmrt.2023.06.047

for its exceptional quality and productivity. Leicht et al. [2] highlighted the widespread recognition of L-PBF's design flexibility and improved mechanical properties, particularly in the aerospace sector. Additionally, Mishra et al. [3] emphasized the potential for optimizing L-PBF, also known as selective laser melting (SLM), by fine-tuning the process parameters to achieve higher efficiency and cavity-free processing.

L-PBF's advantages extend beyond the aerospace and medical sectors, as highlighted by Mishra et al. [4], who further emphasized its ability to produce intricate and lightweight parts with exceptional precision. Neikter et al. [5] specifically pointed out the shorter production times, leading to decreased manufacturing costs. While L-PBF offers numerous advantages, it is crucial to consider the resulting microstructure obtained through this manufacturing process. The unique microstructure achieved through L-PBF sets it apart from conventional processes, with distinct features such as melt pool boundaries, columnar grains, cellular solidification structures, and nano inclusions [2,4,5]. These microstructural elements play a pivotal role in influencing local microscopic deformations, ultimately impacting the macroscopic mechanical properties [5,6]. Palcheo et al. [7] emphasized the importance of meticulous selection of process parameters and scan strategies in L-PBF to achieve desired microstructure and mechanical properties.

Further research has explored the benefits of L-PBF in improving mechanical properties, with Wang et al. [8] attributing enhanced strength to solidification-induced cellular microstructures. Ghosh et al. [9] examined the effects of sensitization on mechanical properties and microstructure in austenitic stainless steel, discussing the depletion of solid solution strengtheners, grain boundary precipitations, and the formation of strain-induced martensite. Smith et al. [10] offers valuable insights into microstructural development, emphasizing the importance of process parameters and alloy composition in shaping the final microstructure of stainless steels. Additionally, the use of inert gases like argon or nitrogen in L-PBF plays a crucial role in eliminating byproducts and air from the process chamber, with high-purity argon further enhancing part toughness [11].

In this study, nitrogen-strengthened austenitic stainless steel alloy 21-6-9 has been investigated. Its name derives from its composition of 21Cr–6Ni–9Mn. The superior properties of this alloy are a result of the low carbon content and the solid solution of nitrogen and manganese [12,13]. Nitrogen (N) and manganese (Mn) are the key elements that provide strength to the alloy. The solid solution of nitrogen in the alloy contributes to enhancing its yield- and tensile strength, compared to nitrogen-lean austenitic stainless steel, and manganese increases the solubility of nitrogen in the alloy. Moreover, alloy 21-6-9 exhibits excellent oxidation resistance and thermal stability at elevated temperatures, while maintaining high strength and toughness at cryogenic temperatures [13]. The 21-6-9 stainless steel alloy finds extensive applications in aerospace, particularly in the fabrication of aircraft engine components, along with its utilization in various other industries [14]. Cobelli et al. [15] focused on improving nitrogen solubility, strengthening mechanisms, and alloying elements' influence in high nitrogen austenitic stainless steels. Their efforts resulted in steels with exceptional strength, corrosion resistance, and cost-effectiveness, suitable for structural applications in industries like automotive and construction. Dai et al. [16] explored the impact of alloying elements and temperature on the strength of cryogenic austenitic steels.

Conventionally produced alloy 21-6-9, such as cast, wrought, and welded, has been extensively studied over a wide range of temperatures. Vandervoort [17], examined the tensile and fracture properties of 21-6-9 stainless steel welded with Inconel 625 at 4 K, finding favorable strength, ductility, and toughness. Elmer et al. [18] studied the mechanical properties of 21-6-9 stainless steel welds at room temperature, providing insights into their behavior under different strains. Torres et al. [19] explored the temperature-dependent behavior of yield strength, ultimate tensile strength, and exceptional ductility of 21-6-9 stainless steel across a temperature range from ambient to 1200 °C. Sakamoto et al. [20] investigated the potential use of nitrogen containing stainless steel for cryogenic applications. Ma et al. [21] focused on the effect of hydrogen on the cryogenic mechanical properties of Cr–Ni–Mn–N austenitic steels. Siewert et al. [22] examined the welding of nitrogen-strengthened austenitic stainless steels and components for cryogenic applications. The significant increase in yield strength in the temperature range of 300 °C to −195 °C was observed as a notable characteristic of the mechanical property variation with temperature [23].

To the authors knowledge, very few studies have been conducted on alloy 21-6-9 processed with L-PBF. Neikter et al. [5] studied the process parameters for L-PBF processing of alloy 21-6-9 and showed that it can be successfully manufactured with good mechanical properties and no significant anisotropic properties. Edin et al. [24] evaluated the thermal stability and tensile properties of an alloy 21-6-9 through microstructural characterization and tensile testing after different annealing temperatures.

High manganese TWIP (twinning induced plasticity) steels exhibit exceptional ductility and high strength at room temperature due to the formation of extensive twins under mechanical loading at room temperature [25–27]. The TWIP phenomenon has been reported for additively manufactured austenitic stainless steel, and it is believed that the good ductility of AM built part is due to the TWIP effect [28–30]. Pham et al. [28] discussed an approach to achieve high strength and ductility in L-PBF produced austenitic stainless steel alloy 316 L by promoting the TWIP effect.

The alloy 21-6-9 has desirable strength and toughness at cryogenic temperatures, which makes it particularly interesting for the aerospace industry. Several studies have been conducted on the performance of conventionally manufactured alloy 21-6-9 at cryogenic temperatures, showing high strength, good ductility, and good fracture toughness [17,21,22]. Alloy 21-6-9 undergoes strain induced martensite formation due to deformation at cryogenic temperature (4K–170 K) [31]. To the authors' knowledge, no study has reported on the cryogenic performance of additively manufactured 21-6-9. This work aims to investigate mechanical properties of L-PBF manufactured alloy 21-6-9 at elevated (750 °C) and cryogenic temperature (77 K) and relate the performance to microstructure evolution.

## 2. Methods

The 21-6-9 stainless steel alloy was manufactured as round bars, using the L-PBF process in argon atmosphere. A summary of the processing parameters is shown in Table 1. There were twelve samples built, with dimensions approximately 6 mm in diameter and 70 mm in length. A schematic of the vertically built L-PBF sample is shown in Fig. 1(a). The chemical composition of the L-PBF-processed bars were evaluated by spark optical emission spectroscopy (spark OES) and X-ray fluorescence (XRF) Niton. In addition, nitrogen and oxygen contents were measured by combustion analysis. The chemical composition of the bars is given in Table 2.

### 2.1. Mechanical testing

Eight samples were machined for tensile testing at room- and cryogenic temperature (77 K) according to ISO 6892-1 [32], see drawing in Fig. 1(b). Four of the samples, for room temperature tensile testing, were heat treated at 750 °C in a Nabertherm N11/H furnace, with holding times 1 h (HT1) and 24 h (HT24), respectively. Four samples were left non-heat treated for reference, two of them for room temperature tensile testing (RT) and two for cryogenic tensile testing. To assure repeatability, two samples were tested under each condition (denoted sq1 and sq2). The test matrix for the tensile testing is shown in Table 3. The sample notations used in the paper are summarized in Table 4.

Room temperature tensile testing was performed in an Instron 1272 under strain control with a max force of 20 kN, in accordance with ASTM-E8. The cryogenic tensile testing was performed at Sandvik AB, according to ISO 6892-3 [33]. The samples were immersed in liquid nitrogen during 20 min before the tests to ensure an even temperature profile and correct temperature (77 K).

### 2.2. Microstructure characterization and fractography

Microstructural characterization was performed with a Nikon SMZ1270 light optical microscope and a scanning electron microscope (JEOL JSM-IT 300). The samples were ground and polished according to conventional polishing methods. For the tensile tested samples, cross-sections were cut approximately 5 mm below the fracture surface for characterization. To reveal the microstructure the samples were etched using 10% oxalic acid at 6 V for 45 s.

The samples were repolished for electron backscatter diffraction (EBSD) analysis in a JEOL IT300LV SEM equipped with an Oxford NordlysMax3 EBSD detector and an Oxford NordlysNano analysis system. The mapping was performed at 15–20 kV and 1.0 nA to obtain information about the crystallographic orientation, with a step size of 0.7 μm.

X-ray diffraction (XRD) runs were performed on all cross-sections to analyze the phase compositions, using a PANalytical Empyrean X-ray diffractometer equipped with a CuKα LFF HR X-ray tube. The XRD patterns were obtained over a 2θ range of 40–100. The data was analyzed by High Score Plus software version 4.9 using the PDF 4 + (2022) database, and Rietveld refinement was performed to estimate the amounts of different crystalline phases.

Fractography was performed on all tensile tested samples with the JEOL JSM-IT 300 scanning electron microscope. All samples were ultrasonically cleaned in acetone prior to evaluation.

**Table 1 – Processing parameters.**

| Name | 21-6-9 |
|---|---|
| Machine | Renishaw AM250 |
| Layer thickness | 60 μm |
| Build atmosphere | Argon |
| Heat treatment | As-built |
| Build direction | 90°, vertically |

### 2.3. Microhardness and nanoindentation

Vickers microhardness measurements were performed with a DURAMIN-40 AC3 microhardness tester using 100 g load and 24 indentations on the following samples: reference, RT sq2, cryogenic sq1, RT(HT1) sq2 and RT(HT24) sq2. Microhardness measurements on RT sq2 and cryogenic sq1 were performed 5 mm below the fracture surface. The microhardness of the heat treated sample RT(HT1) sq2 and RT(HT24) sq2 was measured on the unstrained region.

Nanoindentation tests were performed on the following samples: reference, RT sq2 and cryogenic sq1. The nanoindentation was performed using a NanoTest Vantage high temperature nanoindenter, in 10 × 10 matrices resulting in 100 indentations, with maximum applied load 60 mN.

## 3. Results and discussion

### 3.1. Mechanical properties

#### 3.1.1. Tensile properties

Tensile test results are shown as true stress–strain and engineering stress-strain graphs in Fig. 2(a) and (b) and in Table 5. The obtained yield strengths (YS) at room temperature, ranging from 580 to 650 MPa, are significantly higher than that of traditionally manufactured 21-6-9, which has reported YS values around 300 MPa [18,34]. At cryogenic temperature (77 K), the YS is around 1300 MPa for L-PBF built 21-6-9, which is also higher compared with traditionally manufactured 21-6-9, with reported values around 970 MPa at 77 K [34].

When comparing cryogenic temperature and room temperature, it can be stated that the ultimate tensile strength (UTS) and YS of the L-PBF built 21-6-9 are significantly higher at cryogenic temperature than at room temperature. At cryogenic temperature (77 K), UTS reaches almost 1500 MPa compared to 800 MPa at room temperature, and the YS is around 1300 MPa compared to 650 MPa at room temperature. The elongation at 77 K is drastically reduced to 3–5% (from 37 to 38% at room temperature), indicating an embrittlement of the material. Strain hardening at room temperature is considerable compared with that at cryogenic temperature. There is also an effect of heat treatment on YS, as shown in Table 5. After 1 h heat treatment at 750 °C, there is a reduction of the YS to 582 MPa and 599 MPa, compared to 651 MPa and

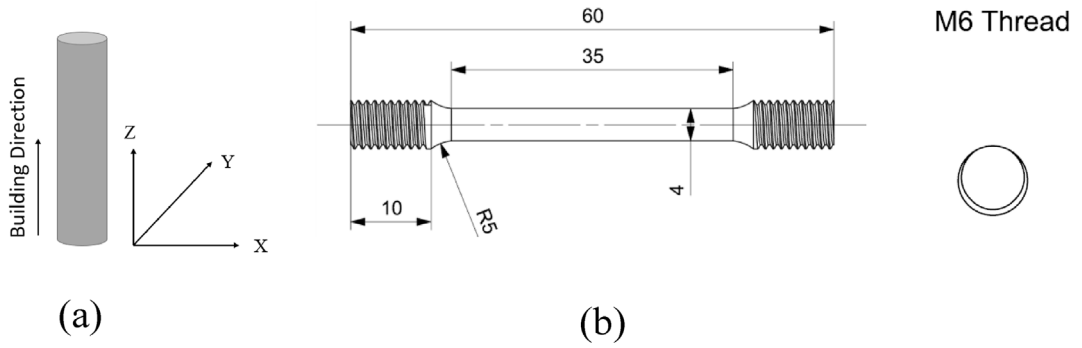


**Fig. 1 – (a) Schematic of the vertically L-PBF built sample, (b) drawing of the sample prepared for tensile test according to ISO 6892-1. Dimensions in mm.**

654 MPa for the non-heat treated samples (RT sq1 and sq 2 samples). The sample with the lower YS (RT (HT1) sq1) broke prematurely due to large defects. Heat treatment of 24 h at 750 °C did not reduce the YS further. The YS values for these samples (RT (HT24) sq1 and sq 2) are 603 MPa and 585 MPa. It can be observed that the UTS remains unaffected by heat treatment at both holding times. The UTS after 1 h of heat treatment is 696 MPa (sample broke prematurely due to defects), and 803 MPa after 24 h. There may be a slight effect of heat treatment on elongation. The elongation values after heat treatment are 34–36% (excluding the sample that broke prematurely), compared to elongation values of 37% and 38% for the non-heat treated samples.

### 3.1.2. *Microhardness and nanoindentation*

Fig. 3(a) shows the microhardness results of one sample tensile tested at room temperature (RT sq2) and one tested at cryogenic temperature (cryogenic sq1), as well as of the reference sample. It can be observed that there are three different hardness levels, with the lowest value obtained for the reference sample with an average hardness of 296 ± 9 HV. The sample tensile tested at cryogenic temperature (77 K) exhibits higher hardness, with an average value of 335 ± 13 HV. The highest hardness is found for the RT sq1 sample, where the average hardness value increases to 406 ± 11 HV.

The microhardness results for the heat treated samples RT (HT1) sq2 and RT (HT24) sq2 and the reference are shown in Fig. 3(b). The reference sample has higher average hardness value (296 ± 9 V) than the heat treated samples. No difference in microhardness can be observed in relation to holding time during heat treatment at 750 °C. The average value of the RT (HT24) sq2 sample is 284 ± 10 HV, and the average value for the RT (HT1) sq2 sample is 283 ± 9 HV. The decrease in microhardness in the heat treated samples compared with the reference sample is likely due to microstructural changes resulting from the heat treatment, such as grain homogeneity and size. In literature the decrease in hardness has been related to a reduction of ferrite phase during heat treatment, as ferrite is significantly harder than austenite [35]. Stress relief is a release of internal energy related to defects in the microstructure, including dislocations. At higher temperatures, atomic diffusion increases, allowing atoms in regions of high stress to move to areas with lower stress. This leads to the relief of internal strain energy and grain coarsening. It is well known that an increased temperature or holding time tend to reduce the microhardness value [36,37].

The nanoindentation results of samples RT sq2, cryogenic sq1 and the reference are shown in Fig. 4. The same trend with three different hardness levels, as was seen for the microhardness results (Fig. 3(a)), can be observed. However, the data is more scattered, especially for RT sq2. Once again, the highest hardness is observed for the RT sq2 sample, while the lowest hardness is found in the reference sample.

The significant increase in hardness of the samples tensile tested at room temperature could be explained by deformation hardening, which leads to the formation of dislocations and twins, as observed in austenitic stainless steels built by laser powder bed fusion, as reported in several studies [28,38,39]. During deformation at room temperature, twinning is often observed in twinning induced plasticity (TWIP) steels. TWIP is an interesting phenomenon that allows the design of high strength and very ductile steels [28–30]. Typically, TWIP steels contain more than 15% Mn and are dependent on carbon content [40]. Since 21-6-9 contains only 8% Mn, a TWIP effect would not be expected in this alloy. However, Pham et al. [28] showed that the L-PBF process can promote a TWIP effect even at lower contents of Mn. Similarly, other studies have indicated that the TWIP effect is induced in austenitic stainless steel 316 L built by additive manufacturing methods with Mn contents as low as 2% [2]. Nitrogen atoms in austenitic steels interact with dislocations and strengthen the alloy, while carbon does not exhibit a similar trend. The amount of nitrogen influences deformation twinning. Nitrogen in solid solution up to and beyond one weight percent significantly increases the yield strength and ultimate tensile

**Table 2 – Chemical composition (wt.%) of 21-6-9.**

| C | Cr | Mn | Ni | Si | N | O | Cu | Ti | Nb | Co | Al | Fe |
|---|---|---|---|---|---|---|---|---|---|---|---|---|
| 0.021 | 19.81 | 8.46 | 7.06 | 0.41 | 0.302 | 0.065 | 0.021 | 0.016 | 0.018 | 0.011 | 0.004 | 63.802 |

**Table 3 – Test matrix.**

| Sample condition | Room temperature | Cryogenic temperature (77 K) |
|---|---|---|
| As-built | 2 | 2 |
| 750 °C; HT1 | 2 | – |
| 750 °C; HT24 | 2 | – |

**Table 4 – Sample notations.**

| | Sample condition |
|---|---|
| Reference | As-built sample, not tensile tested |
| RT | As-built and tensile tested at RT |
| RT(HT1) | Heat treated for 1 h at 750 °C and tensile tested at room temperature |
| RT(HT24) | Heat treated for 24 h at 750 °C and tensile tested at room temperature |
| Cryogenic | As-built and tensile tested at cryogenic temperature (77 K) |

strength [14]. It is widely believed that nitrogen reduces the stacking fault energy, promoting twinning activity during deformation in high-nitrogen steels [28,40,41]. Additionally, deformation twinning likely induces significant plasticity, leading to excellent ductility at room temperature in AM-built austenitic stainless steel [28].

### 3.2. *Material characterization*

#### 3.2.1. *Fractography*

Fig. 5 shows the fracture surfaces of one representative sample for each tensile tested condition. The RT sq2 sample (Fig. 5(a)) shows ductile fracture features, and large shear lips, with a typical cup-and-cone shape proving fully ductile behavior. After heat treatment (RT (HT1) sq2 and RT (HT24) sq2 samples) the fracture surfaces are still ductile, see Fig. 5(b) and (c). Compared with RT sq2 sample the fracture surfaces are flatter, but still show dimples. The sample tested at 77 K (cryogenic sq2, Fig. 5(d)) shows different fracture features. The fracture surface shows a brittle appearance with a flat and smooth surface, with little plastic deformation. Neikter et al. [5] recently observed similar fracture features of L-PBF built 21-6-9 at RT and 750 °C. There were many smaller-sized dimples at RT, whereas at elevated temperatures, fewer and larger dimples were present. Vandervoort [17] discussed the fracture behavior of 21-6-9 weld metal at 4 K (−269 °C). The nature of the fracture surface was basically flat, and it was suggested that the brittle zones may be associated with the martensite transformed.

The fractography results are in line with the mechanical testing results of RT sample and cryogenic sample, see Fig. 2(a and b) and Table 5. RT sample shows ductile behavior, and the cryogenic sample appears more brittle.

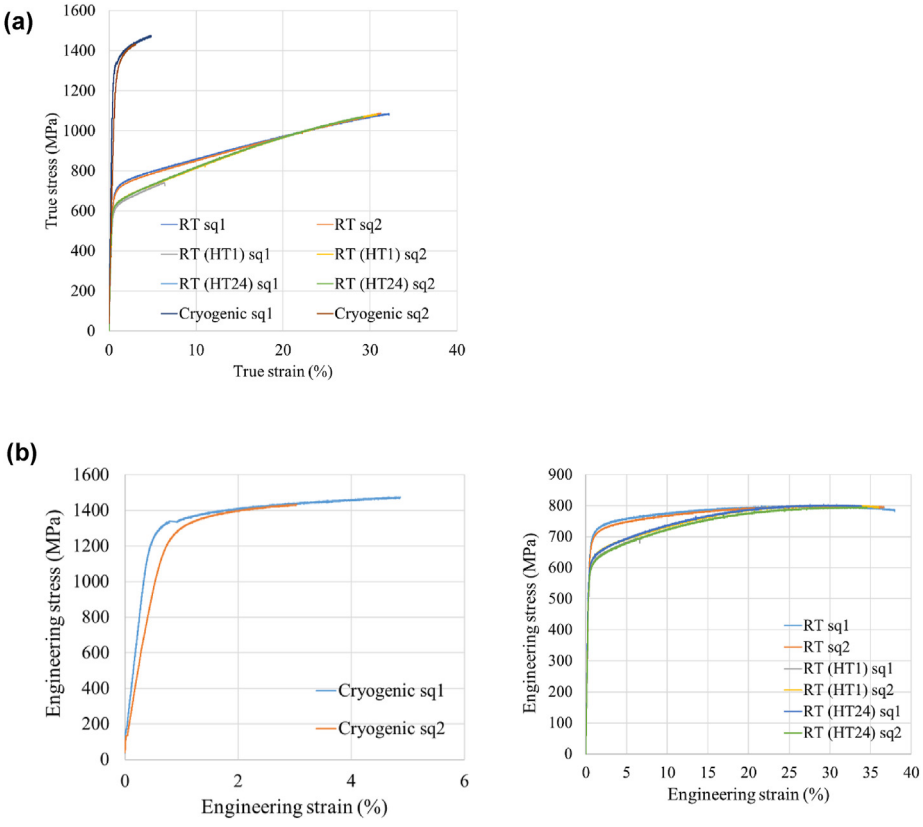


**Fig. 2 – (a). True stress-strain curves of all samples. Sq1 (sequence 1) and sq2 (sequence 2) stand for repetitive samples. (b). Engineering stress-strain curves of cryogenic sample (77 K) (left) and room-temperature (RT) tensile tested samples, as-built and heat treated (HT1 and HT24) (right).**

**Table 5 – Tensile test results, with two repetitive samples at each test condition, labelled sq1 and sq2.**

| | RT sq1 | RT sq2 | RT (HT1) sq1 | RT (HT1) sq2 | RT (HT24) sq1 | RT (HT24) sq2 | Cryogenic sq1 | Cryogenic sq2 |
|---|---|---|---|---|---|---|---|---|
| YS (MPa) | 654 | 651 | 582 | 599 | 603 | 585 | 1306 | 1249 |
| UTS (MPa) | 799 | 800 | 696 | 803 | 804 | 797 | 1472 | 1434 |
| Elongation (%) | 38 | 37 | 7[a] | 36 | 34 | 35 | 4.8 | 3 |

[a] The low elongation was due to large defects.

#### 3.2.2. *Microstructure*

Light optical microscopy images of the microstructure perpendicular to the building direction are shown in Fig. 6 at two different magnifications. Fig. 6(a)–(c) provide overviews, while Fig. 6(d)–(f) are close-up views. The microstructure of the reference sample (Fig. 6(a)–(d)) appears typical for an L-PBF process, with homogeneously distributed grains. In the close-up (Fig. 6(d)) the melt pool boundaries and grain boundaries are highlighted. Fig. 6(b)–(e) shows the microstructure of RT sq2 sample. The melt pools and grain boundaries are visible, as indicated in Fig. 6(e). Plastic deformation from the tensile testing is evident in the microstructure, showing slip lines (an example is marked with an ellipse in Fig. 6(e)). As mentioned above, the elongation of this sample was almost 40% during tensile testing. The presence of slip lines indicates the activation of slip systems during the tensile testing at room temperature, resulting in a higher concentration of dislocations. This explains the significant increase in strain hardening observed in the true stress-strain curve in Fig. 2(a).

Fig. 6(c)–(f) shows the microstructure of the cryogenic sample. In the close-up image (Fig. 6(f)), the deformed microstructure is clearly visible, with two deformed areas indicated with dashed lines. Although the plastic deformation was much lower than that of the samples tested at RT (elongation of 3–5% compared to around 40%), the microstructure exhibits severe deformation, which will be discussed in section 3.2.4.

The light optical microscopy image of the reference sample is displayed in Fig. 7(a), where the grain structure is indicated by arrows. Fig. 7(b) shows the microstructure of the RT (HT1) sample, where the grains are easily distinguishable and marked with black arrows. Some precipitates, visible as black dots along the grain boundaries are present in the microstructure, indicated by white arrows. Fig. 7(c) shows the microstructure of RT (HT24), where the grain boundaries are more clearly visible and marked with black arrow. More precipitates are formed at the grain boundaries, marked with white arrows. According to some researchers, L-PBF-built austenitic stainless steels have no or small amounts of ferrite retained after manufacturing [5,42,43], while other studies have found ferrite in the as-built material [44–46]. During heat treatment, δ-ferrite can transform into austenite and sigma phase [46,47]. The precipitates found in Fig. 7(b) and (c) could therefore be sigma phase forming along the grain boundaries. The sigma phase nucleates at high-energy areas, such as grain boundaries, dislocations, stacking faults, interphases, and chemical heterogeneities in the ferrite phase [48]. The transformation from δ-ferrite to sigma phase can be accelerated when Cr, Si, or Mo efficiently diffuses in δ-ferrite [49]. Thus, the temperature interval in which sigma phase occurs in most commercial steels is between 590 °C and 870 °C [47]. However, the sigma phase is generally undesirable in austenitic stainless steels due to its brittleness and negative impact on mechanical properties [48]. In addition to the risk of transformation to sigma phase, the presence of δ-ferrite can also pose a problem if the material is exposed to cryogenic temperatures, as the ductility of the δ-ferrite phase is greatly affected by temperature [50].

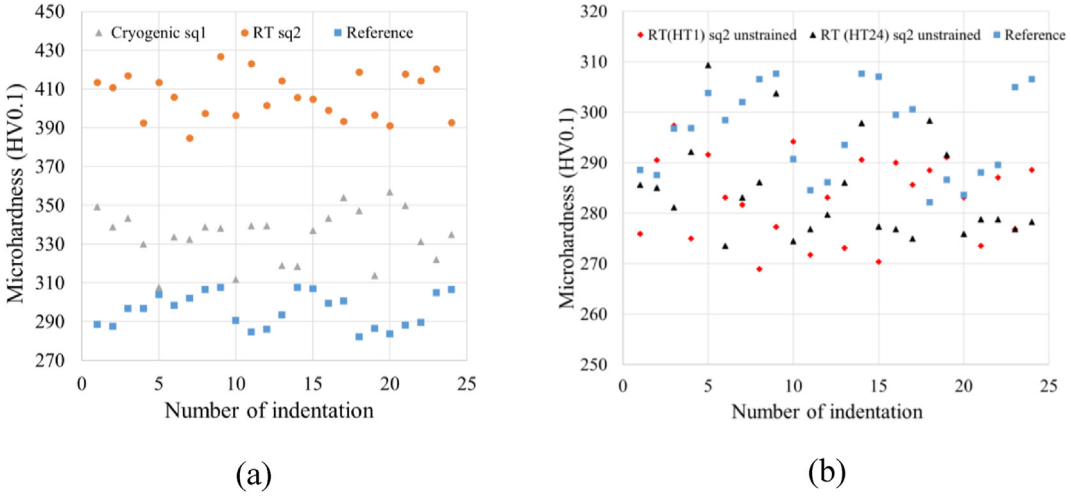


**Fig. 3 – Microhardness of selected samples, compared to reference sample. Microhardness measurements on RT sq2 and cryogenic sq1 were performed 5 mm below the fracture surface. The microhardness of the heat treated sample RT(HT1) sq2 and RT(HT24) sq2 was measured on the unstrained region.**

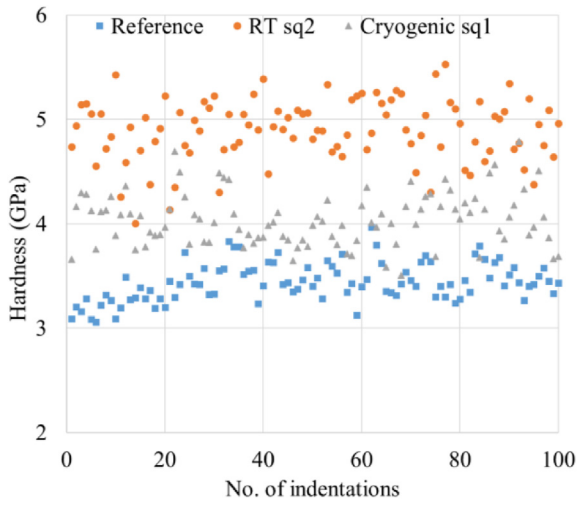


**Fig. 4 – Nanoindentation of reference, RT sq2, and cryogenic sq1.**

### 3.2.3. *XRD*

Figs. 8 and 9 show XRD results for the tensile tested samples, as well as for the reference sample that was not tensile tested. Fig. 8 shows that the reference sample consists of 100% austenite. The RT sq2 sample consists of austenite and small amount of bcc phase. In the cryogenic sample, the XRD confirms the presence of martensite. The amount of martensite was estimated by Rietveld analysis to be 90%, and the rest being austenite.

From Fig. 9 it can be seen that the heat treated samples (RT (HT1) sq2 and RT (HT24) sq2) are mainly austenitic. There are additional diffraction peaks present in the XRD patterns, indicating the emergence of precipitates, such as sigma phase, with a bcc structure. The heat treatment process triggers this precipitation phenomenon and this is in agreement with the assumed precipitation as shown in the microstructure in Fig. 7(b) and (c). Interestingly, despite the observed changes in microstructure and the presence of precipitates, the mechanical properties of the heat treated samples, as depicted in Fig. 2(b), are not significantly affected. In other words, the formation of precipitates, such as sigma phase does not noticeably alter the mechanical behavior of the material.

### 3.2.4. *EBSD*

Fig. 10 shows the EBSD results of the RT sq2 sample, along the building direction. As can be seen from the phase map image in Fig. 10(a), the sample is fully austenitic (red) with small fractions of ferrite (green), which is in good agreement with XRD results in Fig. 8.

In Fig. 10(b) the Inverse Pole Figure (IPF) are shown. The map reveals both larger grains that seem to be $<111>$ and $\langle 101\rangle$ oriented (colored blue and green) and finer grains in between with more random orientation. The color variation within a single grain indicates a difference in grain orientation which in this case could be referred to strain within the material indicating a significant amount of deformation. This is what is also seen in the mechanical properties, in terms of work hardening where the material has significant plastic deformation, see Fig. 2(a). This correlation has been observed in literature, where higher hardness values have been linked to increased crystallographic misorientation in 21-6-9 [23] and other austenitic stainless steel [51].

Fig. 11 displays the EBSD results of the cryogenic sq1 sample. The phase color map (Fig. 11(a)) reveals that the microstructure is mainly martensitic. The sample consists of 92% $\alpha$-martensite (bcc, green) and 8% austenite (red), which aligns with the XRD results, see Fig. 8.

The IPF map in Fig. 11(b) shows the deformed grains in different colors. Interesting to note is the small grains distributed inside the large grains, some indicated with arrows. These small grains have an orientation relationship where the small grain is perpendicular to the $\langle -1-10\rangle$ in the large grain. According to literature, this orientation relationship could have a significant impact on the strain-induced martensitic transformation that occurs during deformation at cryogenic temperature (77 K). The small grains serve as sites of stress concentration initiating the formation of martensitic crystals and depending on the misorientation angle of the grains, influencing the kinetics of the martensite transformation and the resulting martensite variant [24,52–54].

In Fig. 11(c), the band contrast image shows parallel lines, marked by arrows, which are also observable in the microscopic image of the cryogenic sample in Fig. 6(c–f). These parallel lines may be a result of strain induced martensite formation. The appearance of the parallel line areas in Fig. 11(c) and their absence in (b) is an indication of the specific features of martensite, such as long, thin, parallel-sided lines.

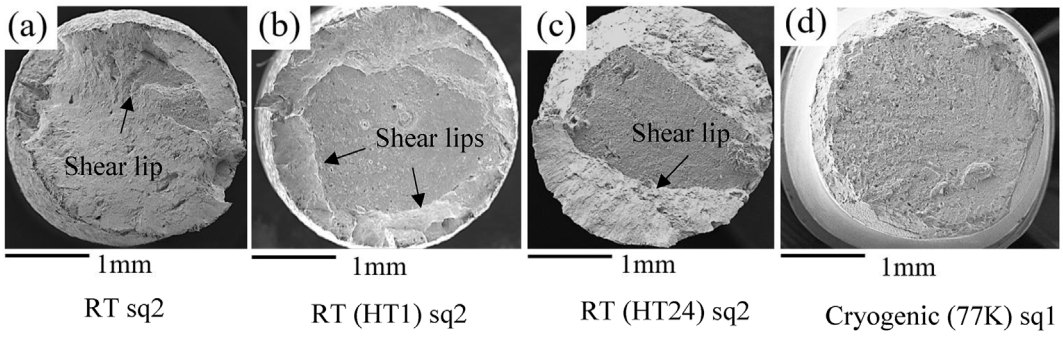


**Fig. 5 – Fracture surfaces of samples tensile tested at room temperature and cryogenic temperature (77 K); (a) RT sq2, (b) RT (HT1) sq2, (c) RT (HT24) sq2, (d) cryogenic (77 K) sq1.**

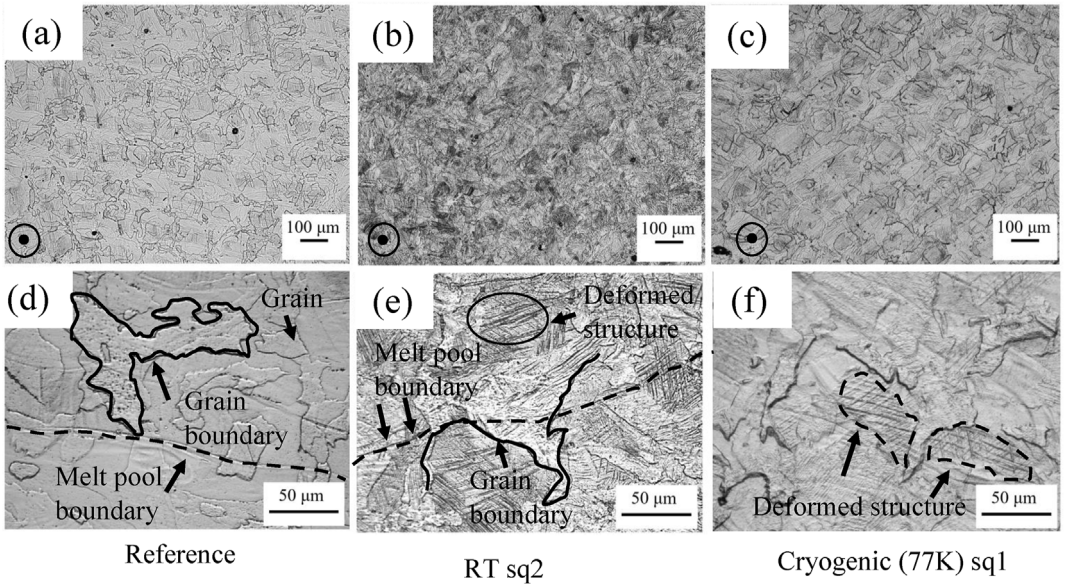


**Fig. 6 – Light optical microscope images; (a) and (d) reference sample; (b) and (e) RT sq2, and (c) and (f) cryogenic sq1. Samples were electrolytically etched with 10% oxalic acid. Building direction is indicated in (a), (b) and (c).**

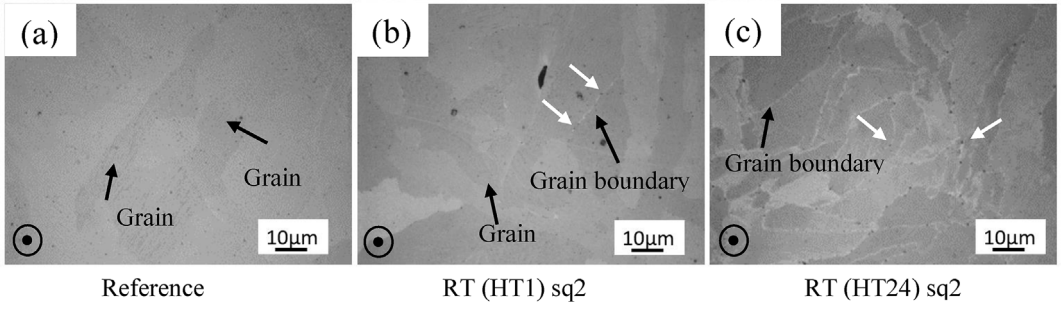


**Fig. 7 – Light optical microscope images; (a) reference, (b) RT (HT1) sq2, (c) RT (HT24) sq2. Samples were electrolytically etched with 50% NaOH.**

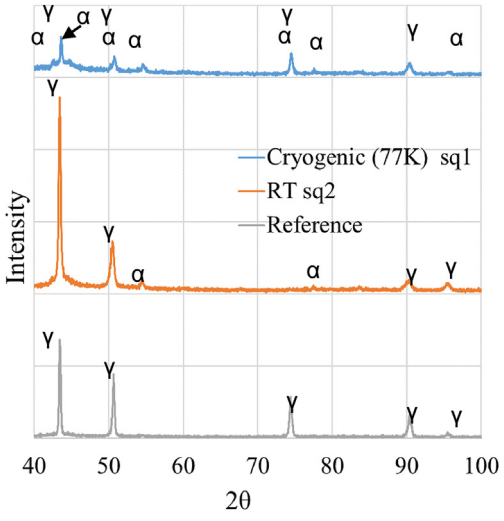


**Fig. 8 – XRD graphs of the reference sample, RT sq2, and cryogenic sq1.**

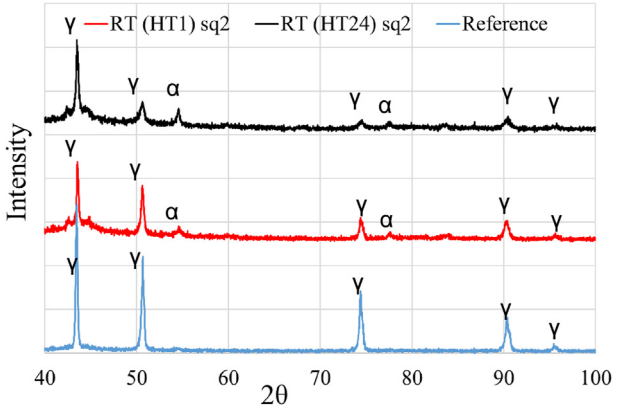


**Fig. 9 – XRD graphs of the reference sample and RT (HT1) sq2 and RT (HT24) sq2 samples.**

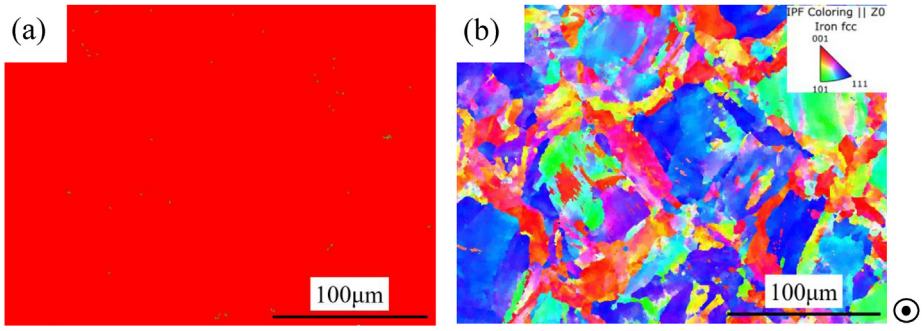


**Fig. 10 – EBSD of RT sq2; (a) Phase map image, austenite in red and small fractions of ferrite in green, (b) IPF map.**

In literature, the number and appearance of these lines have been shown to be impacted by the level of strain applied to the material and the temperature at which the transformation occurs, with higher strain leading to more lines [4,30]. The morphology and distribution of martensite phase determine its hardness. For other alloys at cryogenic temperature, the increase in yield strength is commonly believed to be attributed to the fine sub-cellular microstructure [8,39,55–58] resulting from the L-PBF manufacturing method. This study shows that the same effect is valid also for 21-6-9 alloy after L-PBF manufacturing.

The EBSD data for RT (HT24) sq2 is presented in Fig. 12, where the phase map in Fig. 12(a) reveals an almost entirely austenitic phase with only a small portion of bcc phase, aligning with the XRD results in Fig. 8.

The IPF map in Fig. 12(b) reveals a rather uniform grain size of the larger grains but fewer finer grains in the heat treated sample compared to the non-heat treated samples (Fig. 10(b)). Fig. 12(b) also indicates that the texture is less pronounced but there are still some grains exhibiting a color variation indicating strain within the grains, probably due to deformation. However, even if small variations in microstructure is

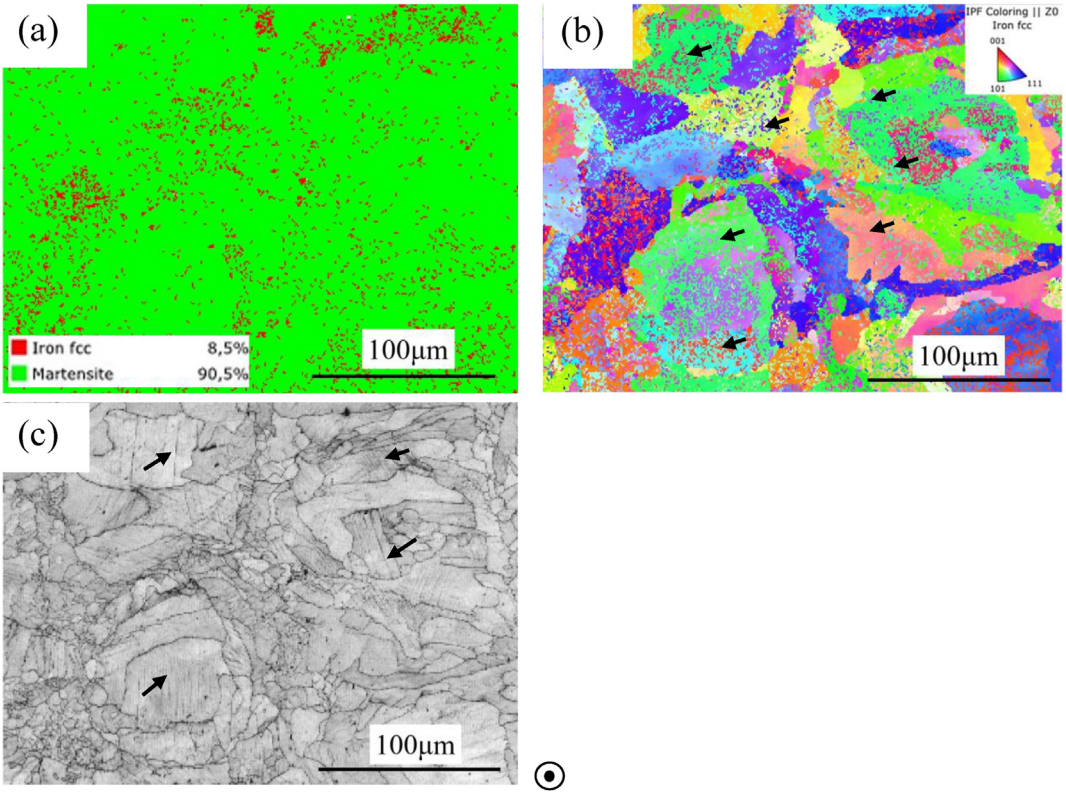


**Fig. 11 – EBSD of cryogenic sq1 sample; (a) Phase map, martensite in green and austenite in red (b) IPF map, (c) band contrast image.**

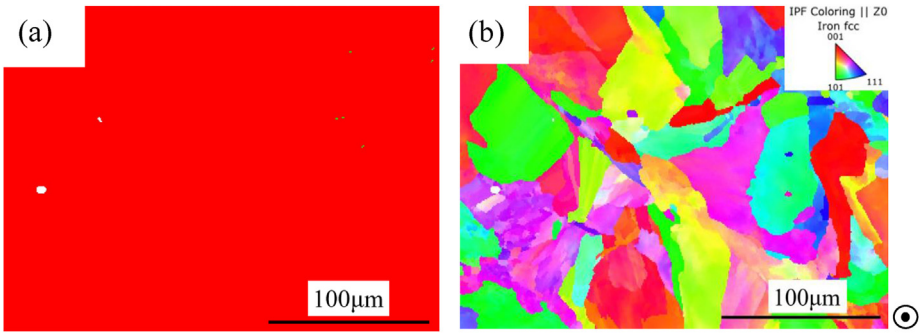


**Fig. 12 – EBSD of HT24 sq2 tested at RT; (a) Phase map, red color shows austenite phase, (b) IPF map.**

observed, the heat treatment does not seem to influence the mechanical properties (Table 5).

The results of this study reveal that the 21-6-9 alloy produced via L-PBF exhibits favorable values of yield strength (YS) and ultimate tensile strength (UTS) at both room- and cryogenic (77 K) temperatures. Tensile testing at 77 K resulted in the formation of strain-induced martensite, leading to an improvement in YS and UTS, but a decrease in ductility. The alloy shows remarkable elongation at room temperature, reaching nearly 40%. It also exhibited a significant amount of strain hardening at room temperature compared to cryogenic temperature.

## 4. Conclusions

In this work, mechanical properties, and microstructure evolution of L-PBF manufactured 21-6-9 were investigated at room- and cryogenic temperature (77 K). Additionally, the impact of heat treatment at 750 °C for 1 h and 24 h on the microstructure and mechanical properties was examined.

- The 21-6-9 alloy produced through L-PBF demonstrates promising properties and could be considered a viable option for aerospace applications.
- At room temperature, L-PBF 21-6-9 has a YS around 650 MPa and the UTS is reaching 800 MPa. Elongation values are around 40%. Compared to conventionally produced 21-6-9, reported in literature, the mechanical properties of the L-PBF-manufactured alloy are superior at room temperature, displaying high yield strength and elongation.
- At cryogenic temperature (77 K), the YS and UTS increase significantly (80%) compared to room temperature, but the elongation decreases severely (90%), probably due to the formation of strain-induced martensite.
- Heat treatments at 750 °C for 1 h and 24 h do not affect the mechanical properties to any large amount. No increase in grain size is visible.
- The microstructure of the L-PBF-manufactured 21-6-9 is consistent with sub-cellular structures typical of austenitic stainless steels after L-PBF production. At room temperature, the observed deformation in the microstructure is caused by strain hardening, while at cryogenic temperatures, the deformation is due to strain-induced martensite.

## Credit authorship contribution statement

P. Mishra: Conceptualization, Methodology, Investigation, Writing –original draft, Writing – review & editing, Visualization. P. Åkerfeldt: Supervision, review & editing. F. Svahn: Writing – review & editing, Supervision. E. Nilsson– review & editing, F. Forouzan– review & editing, M-L. Antti: Writing – review & editing, Supervision.

## Declaration of competing interest

The authors declare that they have no known competing financial interests or personal relationships that could have appeared to influence the work reported in this paper.

## Acknowledgements

The authors would like to express their gratitude to Esa Vuorinen for providing valuable time for discussion. Additionally, the authors acknowledge LUMIA (Luleå Material Imaging and Analysis) for granting access to materials characterization instruments.

## REFERENCES

[1] Moeinfar K, Khodabakhshi F, Kashani-Bozorg SF, Mohammadi M, Gerlich AP. A review on metallurgical aspects of laser additive manufacturing (LAM): stainless steels, nickel superalloys, and titanium alloys. J Mater Res Technol 2022;16:1029–68. https://doi.org/10.1016/j.jmrt.2021.12.039.

[2] Leicht A, Fischer M, Klement U, Nyborg L, Hryha E. Increasing the productivity of laser powder bed fusion for stainless steel 316L through increased layer thickness. J Mater Eng Perform 2021;30:575–84. https://doi.org/10.1007/s11665-020-05334-3.

[3] Mishra P, Ilar T, Brueckner F, Kaplan A. Energy efficiency contributions and losses during selective laser melting. J Laser Appl 2018;30:032304. https://doi.org/10.2351/1.5040603.
[4] Mishra P, Åkerfeldt P, Forouzan F, Svahn F, Zhong Y, Shen Z, et al. Microstructural characterization and mechanical properties of L-PBF processed 316 L at cryogenic temperature. Materials 2021;14:5856. https://doi.org/10.3390/ma14195856.
[5] Neikter M, Edin E, Proper S, Bhaskar P, Nekkalapudi GK, Linde O, et al. Tensile properties of 21-6-9 austenitic stainless steel built using laser powder-bed fusion. Materials 2021;14:4280. https://doi.org/10.3390/ma14154280.
[6] Gong G, Ye J, Chi Y, Zhao Z, Wang Z, Xia G, Chen C. Research status of laser additive manufacturing for metal: a review. J Mater Res Technol 2021;15:855–84. https://doi.org/10.1016/j.jmrt.2021.08.050.
[7] Pacheco V, Marattukalam JJ, Karlsson D, Dessieux L, Van Tran K, Beran P, et al. On the relationship between laser scan strategy, texture variations and hidden nucleation sites for failure in laser powder-bed fusion. Materialia 2022;26:101614. https://doi.org/10.1016/j.mtla.2022.101614.
[8] Wang YM, Voisin T, McKeown JT, Ye J, Calta NP, Li Z, et al. Additively manufactured hierarchical stainless steels with high strength and ductility. Nat Mater 2018;17:63–71. https://doi.org/10.1038/nmat5021.
[9] Ghosh S, Kain V, Ray A, Roy H, Sivaprasad S, Tarafder S, et al. Deterioration in fracture toughness of 304LN austenitic stainless steel due to sensitization. Metall Mater Trans A 2009;40:2938–49. https://doi.org/10.1007/s11661-009-0023-y.
[10] Smith TR, Sugar JD, Marchi CS, Schoenung JM. Microstructural development in DED stainless steels: applying welding models to elucidate the impact of processing and alloy composition. J Mater Sci 2021;56:762–80. https://doi.org/10.1007/s10853-020-05232-y.
[11] Sun Z, Tan X, Tor SB, Chua CK. Simultaneously enhanced strength and ductility for 3D-printed stainless steel 316L by selective laser melting. NPG Asia Mater 2018;10:127–36. https://doi.org/10.1038/s41427-018-0018-5.
[12] Feichtinger HK. Powder metallurgy of high nitrogen steels. Powder Met Internal 1990;22:12–3.
[13] Tech Steel & Materials. Stainless steel 21-6-9, https://www.techsteel.net/alloy/stainless-steel/21-6-9.
[14] Simmons JW. Overview: high-nitrogen alloying of stainless steels. Mater Sci Eng A 1996;207:159–69. https://doi.org/10.1016/0921-5093(95)09991-3.
[15] Cobelli P. Development of ultrahigh strength austenitic stainless steels alloyed with nitrogen. ETH Zurich; 2003. p. 937–42. 426-432.
[16] Dai QX, Wang AD, Cheng XN, Cheng L. Effect of alloying elements and temperature on strength of cryogenic austenitic steels. Mater Sci Eng A 2001;311:205–10. https://doi.org/10.1016/s0921-5093(00)01796-2.
[17] Vandervoort RR. Mechanical properties of inconel 625 welds in 21-6-9 stainless steel at 4K. Cryogenics 1979;19:448–52. https://doi.org/10.1016/0011-2275(79)90053-5.
[18] Elmer JW, Ellsworth GF, Florando JN, Golosker IV, Mulay RP. Microstructure and mechanical properties of 21-6-9 stainless steel electron beam welds. Metall Mater Trans A 2017;48:1771–87. https://doi.org/10.1007/s11661-017-3996-y.
[19] Torres SG, Henshall GA. Tensile properties of 21-6-9 stainless steel at elevated temperatures (No. UCRL-ID-114590). California, US: Lawrence Livermore National Lab.; 1993.
[20] Sakamoto T, Nakagawa Y, Yamauchi I, Zaizen T, Nakajima H, Shimamoto S. Nitrogen-containing 25Cr-13Ni stainless steel as a cryogenic structural material. In: Clark AF, Reed RP, editors. Advances in cryogenic engineering materials. Boston, MA: Springer; 1984. p. 137–44.
[21] Ma LU, Liang GJ, Tan J, Rong LJ, Li YY. Effect of hydrogen on cryogenic mechanical properties of Cr-Ni-Mn-N austenitic steels. J Mater Sci Technol 1999;15:67–70.
[22] Siewert TA, McCowan CN. Welding for cryogenic service. In: ASM handbook. Ohio: ASM International; 1993. p. 1016–9. https://doi.org/10.31399/asm.hb.v06.a0001464.
[23] Kassner ME, Geantil P. Yield stress of 21-6-9 stainless steel over very wide ranges of strain rates and temperatures. J Mater Eng Perform 2012;21:69–73. https://doi.org/10.1007/s11665-010-9818-7.
[24] Edin E, Svahn F, Neikter M, Åkerfeldt P. Stress relief heat treatment and mechanical properties of laser powder bed fusion built 21-6-9 stainless steel. Mater Sci Eng A 2023;868:144742. https://doi.org/10.1016/j.msea.2023.144742.
[25] Pozuelo M, Wittig JE, Jiménez JA, Frommeyer G. Enhanced mechanical properties of a novel high-nitrogen Cr-Mn-Ni-Si austenitic stainless steel via TWIP/TRIP effects. Metall Mater Trans A 2009;40:1826–34. https://doi.org/10.1007/s11661-009-9863-8.
[26] Yuan X, Chen L, Zhao Y, Di H, Zhu F. Dependence of grain size on mechanical properties and microstructures of high manganese austenitic steel. Procedia Eng 2014;81:143–8. https://doi.org/10.1016/j.proeng.2014.09.141.
[27] Fujiyama K, Mori K, Matsunaga T, Kimachi H, Saito T, Hino T, et al. Creep-damage assessment of high chromium heat resistant steels and weldments. Mater Sci Eng A 2009;510–511:195–201. https://doi.org/10.1016/j.msea.2008.08.045.
[28] Pham MS, Dovgyy B, Hooper PA. Twinning induced plasticity in austenitic stainless steel 316L made by additive manufacturing. Mater Sci Eng A 2017;704:102–11. https://doi.org/10.1016/j.msea.2017.07.082.
[29] Haase C, Bültmann J, Hof J, Ziegler S, Bremen S, Hinke C, et al. Exploiting process-related advantages of selective laser melting for the production of high-manganese steel. Materials 2017;10:56. https://doi.org/10.3390/ma10010056.
[30] Shen YF, Li XX, Sun X, Wang YD, Zuo L. Twinning and martensite in a 304 austenitic stainless steel. Mater Sci Eng A 2012;552:514–22. https://doi.org/10.1016/j.msea.2012.05.080.
[31] Pilhagen J. A literature review of the stainless steel 21-6-9 and its potential for sandwich nozzles. Master's Thesis. Luleå, Sweden: Luleå University of Technology; 2007.
[32] ISO, International Standard. 6892-1. Metallic materials-tensile testing-part 1: method of test at room temperature. Geneva, Switzerland: International Organization for Standardization; 2009.
[33] ISO. 6892-3. Metallic materials—tensile testing—part 3—method of test at low temperature. Geneva, Switzerland: International Organization for Standardization; 2015.
[34] Alexander DJ, Goodwin GM. Thick-section weldments in 21-6-9 and 316LN stainless steel for fusion energy applications. J Nucl Mater 1992;191–194:691–5. https://doi.org/10.1016/0022-3115(92)90561-x.
[35] Salarvand V, Sohrabpoor H, Mohammadi MA, Nazari M, Raghavendra R, Mostafaei A, et al. Microstructure and corrosion evaluation of as-built and heat-treated 316L stainless steel manufactured by laser powder bed fusion. J Mater Res Technol 2022;18:4104–13. https://doi.org/10.1016/j.jmrt.2022.03.156.
[36] Tascioglu E, Karabulut Y, Kaynak Y. Influence of heat treatment temperature on the microstructural, mechanical, and wear behavior of 316L stainless steel fabricated by laser powder bed additive manufacturing. Int J Adv Manuf Technol 2020;107:1947–56. https://doi.org/10.1007/s00170-020-04972-0.
[37] Tucho WM, Cuvillier P, Sjolyst-Kverneland A, Hansen V. Microstructure and hardness studies of inconel 718 manufactured by selective laser melting before and after

solution heat treatment. Mater Sci Eng A 2017;689:220–32. https://doi.org/10.1016/j.msea.2017.02.062.
[38] Liu L, Ding Q, Zhong Y, Zou J, Wu J, Chiu Y-L, et al. Dislocation network in additive manufactured steel breaks strength–ductility trade-off. Mater Today 2018;21:354–61. https://doi.org/10.1016/j.mattod.2017.11.004.
[39] Qiu C, Kindi MA, Aladawi AS, Hatmi IA. A comprehensive study on microstructure and tensile behaviour of a selectively laser melted stainless steel. Sci Rep 2018;8:1–16. https://doi.org/10.1038/s41598-018-26136-7.
[40] Grässel O, Krüger L, Frommeyer G, Meyer LW. High strength Fe–Mn–(Al, Si) TRIP/TWIP steels development — properties — application. Int J Plast 2000;16:1391–409. https://doi.org/10.1016/s0749-6419(00)00015-2.
[41] Hänninen H, Romu J, Ilola R, Tervo J, Laitinen A. Effects of processing and manufacturing of high nitrogen-containing stainless steels on their mechanical, corrosion and wear properties. J Mater Process Technol 2001;117:424–30. https://doi.org/10.1016/s0924-0136(01)00804-4.
[42] Becker L, Boes J, Lentz J, Cui C, Uhlenwinkel V, Steinbacher M, et al. Quantification of extremely small-structured ferritic-austenitic phase fractions in stainless steels manufactured by laser powder bed fusion. Materialia 2022;22:101393. https://doi.org/10.1016/j.mtla.2022.101393.
[43] Saeidi K, Gao X, Zhong Y, Shen ZJ. Hardened austenite steel with columnar sub-grain structure formed by laser melting. Mater Sci Eng A 2015;625:221–9. https://doi.org/10.1016/j.msea.2014.12.018.
[44] Sun Z, Tan X, Tor SB, Yeong WY. Selective laser melting of stainless steel 316L with low porosity and high build rates. Mater Des 2016;104:197–204. https://doi.org/10.1016/j.matdes.2016.05.035.
[45] Kurzynowski T, Gruber K, Stopyra W, Kuźnicka B, Chlebus E. Correlation between process parameters, microstructure and properties of 316 L stainless steel processed by selective laser melting. Mater Sci Eng A 2018;718:64–73. https://doi.org/10.1016/j.msea.2018.01.103.
[46] Kamariah MSIN, Harun WSW, Khalil NZ, Ahmad F, Ismail MH, Sharif S. Effect of heat treatment on mechanical properties and microstructure of selective laser melting 316L stainless steel. IOP Conf Ser Mater Sci Eng 2017;257:012021. https://doi.org/10.1088/1757-899x/257/1/012021.
[47] Almaida GG, Mirsada O, Sulejman M. Effect of the delta-ferrite content on the tensile properties in Nitronic 60 steel at room temperature and 750 °C. Mater Technol 2012;46:519–23.
[48] Biezma MV, Martin U, Linhardt P, Ress J, Rodríguez C, Bastidas DM. Non-destructive techniques for the detection of sigma phase in duplex stainless steel: a comprehensive review. Eng Fail Anal 2021;122:105227. https://doi.org/10.1016/j.engfailanal.2021.105227.
[49] Hsieh CC, Wu W. Overview of intermetallic sigma (σ) phase precipitation in stainless steels. ISRN Metall 2012;2012:732471. https://doi.org/10.5402/2012/732471.
[50] Wegrzyn T. Delta ferrite in stainless steel weld metals. Weld Int 1992;6:690–4. https://doi.org/10.1080/09507119209548267.
[51] Chen Y, Zuo X, Zhang W, Hao Z, Li Y, Luo Z, et al. Enhanced strength-ductility synergy of bimetallic laminated steel structure of 304 stainless steel and low-carbon steel fabricated by wire and arc additive manufacturing. Mater Sci Eng A 2022;856:143984. https://doi.org/10.1016/j.msea.2022.143984.
[52] Heidarzadeh A, Neikter M, Enikeev N, Cui L, Forouzan F, Mousavian RT. Post-treatment of additively manufactured Fe–Cr–Ni stainless steels by high pressure torsion: TRIP effect. Mater Sci Eng A 2021;811:141086. https://doi.org/10.1016/j.msea.2021.141086.
[53] Li J, Qu H, Bai J. Grain boundary engineering during the laser powder bed fusion of TiC/316L stainless steel composites: new mechanism for forming TiC-induced special grain boundaries. Acta Mater 2022;226:117605. https://doi.org/10.1016/j.actamat.2021.117605.
[54] Lobanov ML, Pastukhov VI, Redikul'tsev AA. Effect of special boundaries on $\gamma \rightarrow \alpha$ transformation in austenitic stainless steel. Phys Met Metallogr 2021;122:396–402. https://doi.org/10.1134/s0031918x21040050.
[55] Hong Y, Zhou C, Zheng Y, Zhang L, Zheng J, Chen X, et al. Formation of strain-induced martensite in selective laser melting austenitic stainless steel. Mater Sci Eng A 2019;740–741:420–6. https://doi.org/10.1016/j.msea.2018.10.121.
[56] Shamsujjoha M, Agnew SR, Fitz-Gerald JM, Moore WR, Newman TA. High strength and ductility of additively manufactured 316L stainless steel explained. Metall Mater Trans A 2018;49:3011–27. https://doi.org/10.1007/s11661-018-4607-2.
[57] Wang X, Muñiz-Lerma JA, Sánchez-Mata O, Shandiz MA, Brochu M. Microstructure and mechanical properties of stainless steel 316L vertical struts manufactured by laser powder bed fusion process. Mater Sci Eng A 2018;736:27–40. https://doi.org/10.1016/j.msea.2018.08.069.
[58] Kong D, Dong C, Wei S, Ni X, Zhang L, Li R, et al. About metastable cellular structure in additively manufactured austenitic stainless steels. Addit Manuf 2021;38:101804. https://doi.org/10.1016/j.addma.2020.101804.